

ARTICLE

DOI: [10.1038/s42005-018-0064-x](https://doi.org/10.1038/s42005-018-0064-x)

OPEN

Fast linear electro-optic effect in a centrosymmetric semiconductor

Mathias Berciano¹, Guillaume Marcaud¹, Pedro Damas¹, Xavier Le Roux¹, Paul Crozat¹, Carlos Alonso Ramos¹, Diego Pérez Galacho¹, Daniel Benedikovic¹, Delphine Marris-Morini¹, Eric Cassan¹ & Laurent Vivien¹

Silicon photonics, considered as a major photonic platform for optical communications in data centers, is today also developed for others applications including quantum photonics and sensing. Advanced silicon functionalities based on optical nonlinearities are then required. As the presence of inversion symmetry in the Si crystal structure prevents the exploitation of second-order optical nonlinearities, the generation of strain gradients in Si by a stressed material can be considered. However, due to the semiconductor nature of silicon with the presence of carriers, no clear evidence of second-order nonlinearities have been reported yet. Here we report an experimental demonstration of high-speed Pockels effect in silicon waveguides at 1550 nm. Additionally, a theoretical model is developed to describe its frequency behavior. A second-order nonlinear susceptibility $\chi_{xxy}^{(2)}$ of $-1.8 \pm 0.2 \text{ pm V}^{-1}$ is then experimentally determined. These results pave the way for the development of fast linear electro-optic effect for advanced silicon photonics devices.

¹Centre for Nanoscience and Nanotechnology (C2N), CNRS, Université Paris-Sud, Université Paris-Saclay, UMR 9001, 91405 Orsay Cedex, France. Correspondence and requests for materials should be addressed to M.B. (email: mathias.berciano@c2n.upsaclay.fr)

The development of silicon photonics has the purpose of improving data communications by combining photonics and electronics in the same integrated circuits¹. By taking advantage of the high index contrast, provided by the silicon-on-insulator (SOI) platform, compact devices can be fabricated with the well-established complementary metal-oxide-semiconductor (CMOS) fabrication techniques used in microelectronics while reducing fabrication costs. Besides, silicon has proven to be an excellent material for the realization of a wide range of photonic devices. However, the inversion symmetry present in its crystal structure² prevents the exploitation of second-order optical nonlinearities, a set of effects that would be of great interest for silicon photonics.

Indeed, non-centrosymmetric materials are well known to exhibit second-order electric susceptibility ($\chi^{(2)}$) properties including second-harmonic generation and a linear electro-optic effect, i.e., Pockels effect for a large range of applications: optical communication systems, quantum photonics, security, aerospace, biology...^{3–6} Among all, lithium niobate (LiNbO₃) is the most frequently used due to its large $\chi^{(2)}$ coefficients, providing inter alia, efficient, and high-speed electro-optic modulation. However, for the purpose of data communication applications, lower costs, higher compactness, and higher fabrication yields on chip are required, as permitted with silicon.

The inversion symmetry limitation may be overcome by straining the silicon lattice. Indeed, a non-uniform strain applied to the crystal induces displacements of the silicon atoms, which break its centrosymmetry. The new atomic arrangement plays an important role in the generated second-order polarization, which in turn, directly intervenes in the components of the $\chi^{(2)}$ tensor. This technique to generate $\chi^{(2)}$ in silicon through the use of strain has been explored theoretically^{7–13}, as well as experimentally^{14–19} in the past years.

Indeed, several experimental demonstrations have been reported, attempting the estimations of the strain-induced $\chi^{(2)}$ through the Pockels effect. This gave rise to high values of second-order electric susceptibility, in many cases competing to those typically achievable in lithium niobate^{15–17}. However, without considering the inherent semiconductor nature of silicon, such analysis of a linear electro-optic effect could not account for realistic Pockels coefficients. Recently, it has been demonstrated that free carriers play a critical role on the electro-optic effect in strained silicon waveguides. By applying an electric field to a silicon waveguide, the free-carrier concentration and distribution are indeed changed, which results in a variation of the refractive index due to the plasma-dispersion effect^{20,21}. Furthermore, it has been reported that the linear electro-optic effect detected in strained silicon waveguides was induced by charging centers in the SiN stress overlayer, which moves the silicon waveguide directly into an inversion regime, where the electron concentration grows linearly with the voltage^{22–24}. This result has deep consequences for the interpretation of the electro-optic effect in strained silicon waveguides, particularly in the conclusion that there are two main electro-optic (EO) effects that jointly contribute to the total change in effective mode index (Δn_{eff}) in a strained silicon waveguide. These effects are: the plasma-dispersion effect ($\Delta n_{\text{eff},c}$) induced by carriers and the strain-induced Pockels effect ($\Delta n_{\text{eff},p}$). Therefore, the overall electro-optic effect may be written as follows:

$$\Delta n_{\text{eff}} = \Delta n_{\text{eff},c} + \Delta n_{\text{eff},p}. \quad (1)$$

The inclusion of the free-carrier effect into the electro-optic description of strained silicon waveguides has led to the conclusion that the experimental results previously reported on the strain-induced $\chi^{(2)}$ in silicon have been erroneously interpreted in

the characterization of strained silicon waveguides²². Consequently, one of the recent challenges is to experimentally demonstrate the strain-induced Pockels effect by isolating both electro-optic effects, alongside distinctive validation of the existence of Pockels effect in strained silicon waveguides. It is well-known that an electric field (induced by a voltage) applied into the Si waveguide automatically affects the carrier distribution, inducing a direct change in the effective index of the guided mode. However, these intrinsic changes in carrier distribution also modify the distribution of the electrical field inside the silicon waveguide, thereby significantly affecting the electro-optic efficiency induced by Pockels effect²⁵. The carrier evolution under a bias voltage induces a screening effect, which makes the probing of the Pockels effect and a subsequent estimation of $\chi^{(2)}$ coefficient in strained silicon waveguides vastly challenging.

Nevertheless, the two effects that come into play have very distinct origins, which results in different physical properties that can be advantageously exploited during the experimental characterizations. It is well-known that the Pockels effect is an ultrafast electro-optic effect, with a response time of the order of femtoseconds²⁶, while the free-carrier effect involved in the waveguiding system (i.e., into Si waveguide, at the interfaces, and into the stress layer) is typically characterized by a comparatively lower response time of nanoseconds, corresponding to the carriers recombination time^{27,28}. Hence, when increasing the frequency in the microwave domain, the contribution of carriers to modulation becomes negligible, thereby leaving the Pockels effect to be solely responsible for overall electro-optic modulation.

In this work, we demonstrate fast electro-optic properties based on the Pockels effect at a wavelength of about 1550 nm. Its efficiency according to the direction of light propagation with respect to the crystal lattice is also experimentally and theoretically studied. High-speed electro-optic responses are demonstrated using different-oriented traveling-wave Mach-Zehnder interferometers (TWMZI) in order to dissociate both fundamental contributions, i.e., carrier and Pockels effects. Alongside the high-speed Pockels-based electro-optic characterizations, a model is developed to fit the results obtained and retrieve critical parameters needed to describe the second-order nonlinear susceptibility in a strained silicon waveguide.

Results

Characteristics of devices. A set of 10 asymmetric Mach-Zehnder interferometers (MZI), of length $L_{\text{arm}} = 2$ mm and a delay $\Delta L = 60$ μm between the two arms, with different orientation angles φ ranging between 0° and 45° (with 5° step) according to the wafer orientation notch along the [011] axis, was fabricated (Fig. 1). The different angled waveguides were designed to work in a single-mode condition with a transverse electric (TE) polarization. A cross-sectional view of the electric field intensity of the fundamental TE mode is shown in Fig. 2. The sample was covered by a silicon nitride (SiN) stressed thin film, with a level of internal stress $\sigma_i = -1.3$ GPa to induce strain gradients in silicon waveguides. Coplanar electrodes were placed on top of the MZI to generate an electric field under an applied voltage (See Methods for fabrication details).

Frequency domain characterizations. The efficiency of a strain-induced Pockels effect in silicon was determined in a high-speed regime by taking the advantage of the traveling wave electrodes placed above the MZI in order to propagate an AC electric signal at microwave frequency (see Methods for high-speed measurements details). In this frequency range, it is necessary to take into account the waving behavior of the driving electric signal and properly optimize its interaction with the optical wave. The

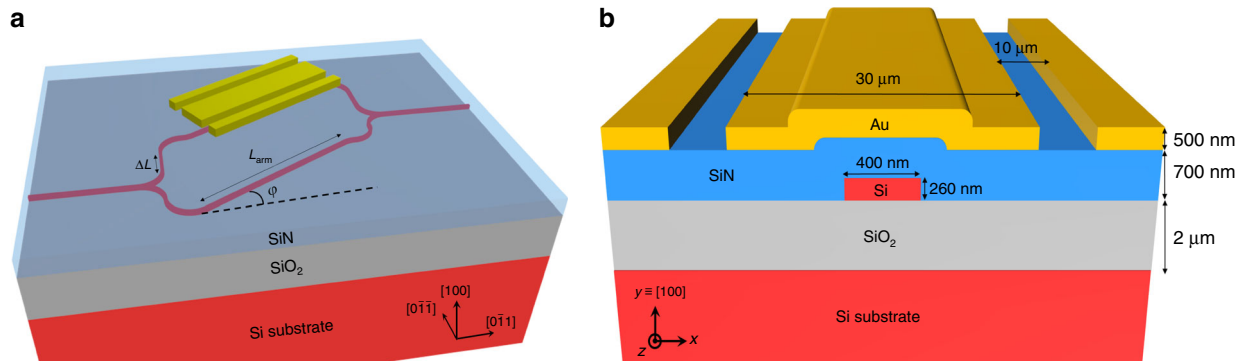


Fig. 1 Schematic views of the waveguiding device. **a** Top view of an angled Mach-Zehnder interferometer (MZI), with an orientation lying between the $[0\bar{1}1]$ and $[0\bar{1}0]$ silicon axis. **b** Cross-sectional view of a silicon waveguide strained by SiN obtained in one arm of a traveling-wave Mach-Zehnder interferometers (TWMZI). L_{arm} is the length of the arms, φ is the angle of the waveguide according to the $[0\bar{1}1]$ crystallographic axis, and ΔL is the delay between the two arms

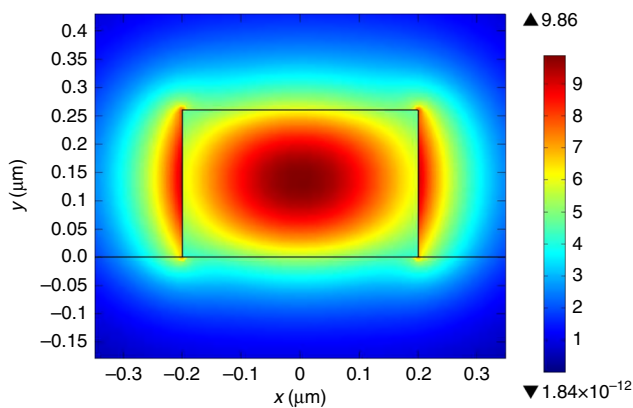


Fig. 2 Electric field intensity (in V m^{-1}) of the fundamental transverse electric (TE) optical mode of the Si waveguide

electrodes were designed to satisfy the impedance matching and low transmission loss conditions to ensure the probing of Pockels effect. For each angled MZI, the electro-optic spectra at a quadrature point λ_{opt} (3 dB below the maximum transmission where the MZI transfer function is linearized) have been measured and analyzed. In addition, a DC bias V_{DC} between -15 V and $+15\text{ V}$ was applied to investigate the influence of carrier distribution from depletion to inversion regimes in frequency domain.

Varying the DC bias from $+15\text{ V}$ to -15 V , a noticeable variation of the optical responses between 100 MHz and about 3 GHz was measured, while the electrical response remained unchanged at higher frequencies (beyond 3 GHz), as shown in Fig. 3 with the 40° MZI. Similar behaviors were also observed at all other angles.

The variation of the electro-optic signal in the low-frequency regime with respect to the DC bias is attributed to variable modulation efficiencies in view of the different regimes of carriers in silicon. As a matter of fact, for reverse bias, free carriers progressively enter to the depletion regime, in which their re-distribution is more easily affected under an AC voltage, as shown in Fig. 4. As a consequence, this leads to stronger variations of the electric field within the silicon waveguide, as shown in Fig. 5.

Conversely, for forward bias, the inversion regime is reached and the re-distribution of free carriers is less affected by an AC voltage. This reduces the electric field re-distribution in the silicon waveguide and leads to lower RF responses. Furthermore, at the given low-carrier distribution change obtained, plasma-dispersion effect has a weak contribution on the electro-optic response. Besides at high-frequency regime, the electro-optic

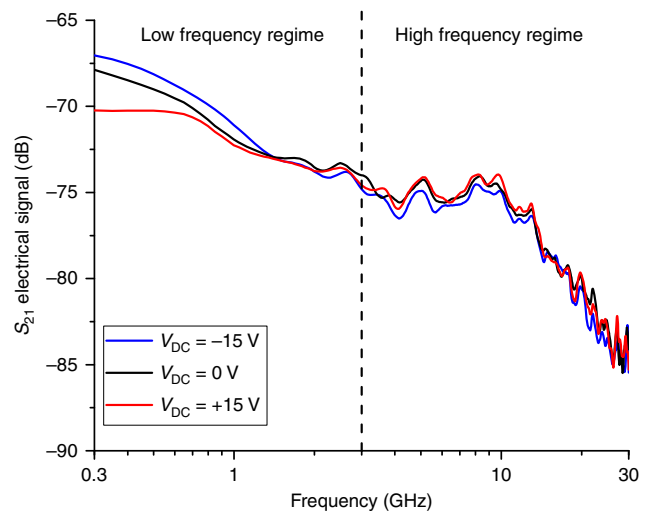


Fig. 3 S_{21} electrical signal of electro-optic (EO) effect, obtained at different DC bias V_{DC} , as a function of the frequency for the 40° Mach-Zehnder interferometer (MZI). Only the electro-optic response in the low-frequency regime is affected by a DC bias change. The ripples typically observed between 3 GHz and 10 GHz are attributed to the radio frequency (RF) setup and were also observed during electrical characterizations. A signal-to-noise ratio above 20 dB was obtained on all traveling-wave Mach-Zehnder interferometers (TWMZI)

response (with respect to the DC bias) is unchanged. This can be explained by the fact that at such frequencies free carriers can no longer keep up the fast voltage variations, and their distributions in the waveguide remain unchanged. Consequently, the measured responses from about 3 GHz is attributed to the Pockels effect. Finally, the decreasing of the signal beyond 10 GHz is explained by the group velocity mismatch between the microwave and the optical signals (as will be explained later).

Silicon being a crystal, different $\chi^{(2)}$ values are expected along its crystallographic axis. Then, at a given forward DC bias ($+15\text{ V}$) to reduce the impact of carriers on the electro-optic behaviors at low frequency, the effect of the orientation angle of the MZI according to the crystallographic directions φ has been studied (Fig. 1). This angle variation allowed studying the evolution of the Pockels effect for different strain gradient conditions. Fig. 6 presents the electro-optic response as a function of the frequency for 10° and 40° TWMZI. For similar electrical and optical input signals, we noticed a difference of the response level, while the overall behavior remained identical.

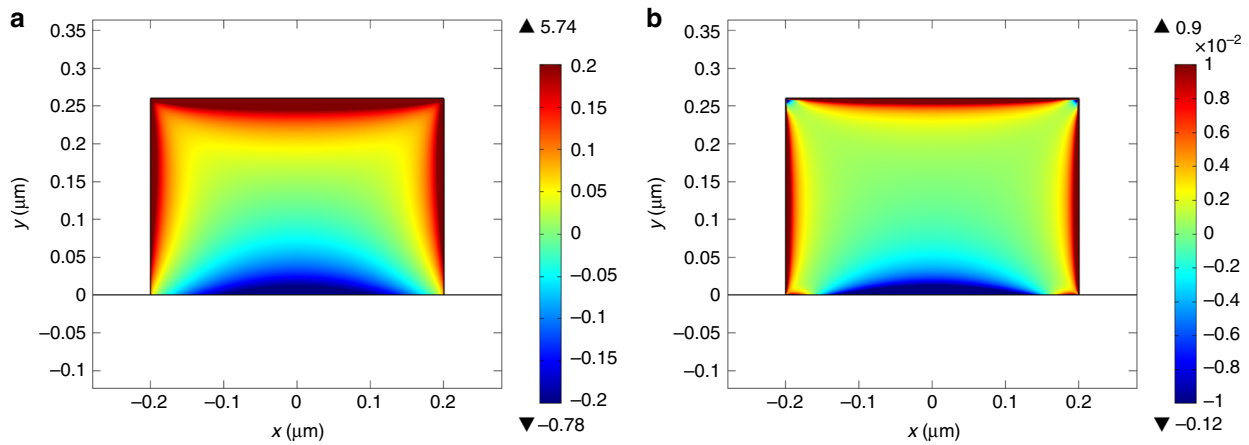


Fig. 4 Electron concentration variation under an AC peak voltage $V_{AC}^P = 10$ V at 300 MHz for different DC bias V_{DC} . **a** Logarithmic scale electron concentration variation (in m^{-3}) when $V_{DC} = -15$ V, corresponding to the depletion regime. The re-distribution of carriers in this regime is more easily affected by an AC voltage. **b** Logarithmic scale electron concentration variation (in m^{-3}) when $V_{DC} = +15$ V, corresponding to the inversion regime. Compared with the depletion regime, the re-distribution of carriers is less affected by the AC voltage (one order of magnitude difference in logarithmic scale between (a) and (b))

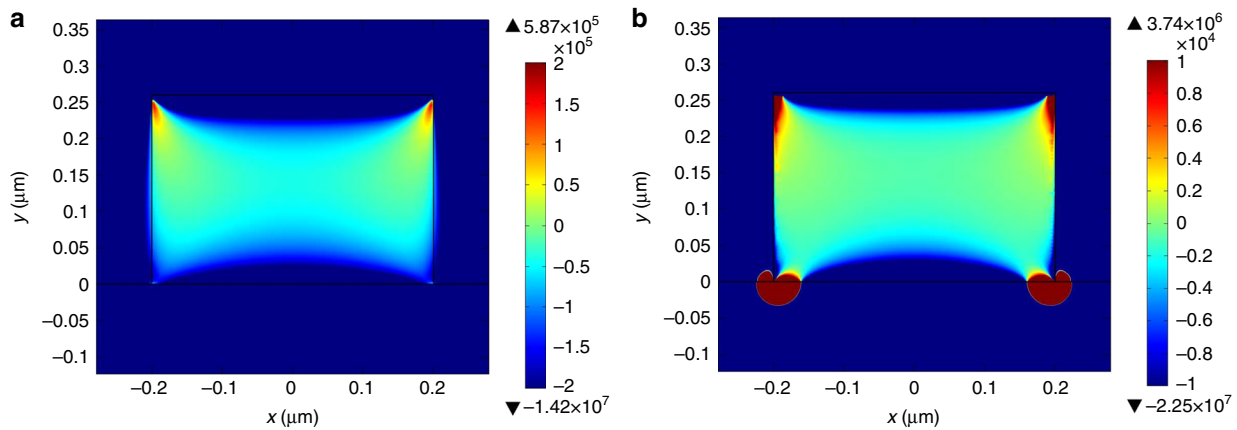


Fig. 5 Vertical electric field variations under an AC peak voltage $V_{AC}^P = 10$ V at 300 MHz for different DC bias V_{DC} . **a** Vertical electric field (in $V.m^{-1}$) change when $V_{DC} = -15$ V. The electric field variation is stronger in this regime, which explains the greater electro-optic response in this frequency range. **b** Vertical electric field change (in $V.m^{-1}$) when $V_{DC} = +15$ V

This difference of the response level with respect to the orientation angle φ , is illustrated in Fig. 7 at 15 GHz. A clear increase in Pockels response was observed when the orientation angle increased, proving that the crystallographic directions play an important role in second-order nonlinear process efficiency.

Theoretical analysis of the Pockels effect. Due to silicon mechanical anisotropy (see Methods), higher strain gradients and then higher $\chi^{(2)}$ coefficients, are obtained when the angle φ increases. In addition, it has been previously shown¹³ that any $\chi_{ijk}^{(2)}$ component can be expressed as a linear combination of the strain gradient components $\eta_{mnl} = \frac{d\varepsilon_{mnl}}{dl}$ (i.e., the variation of the deformation ε_{mnl} along the direction l in the xyz coordinate system shown in Fig. 1):

$$\chi_{ijk}^{(2)}(\varphi) = \sum_{mnl} \Gamma_{ijk,mnl} \eta_{mnl}(\varphi) \quad (2)$$

where the coefficients $\Gamma_{ijk,mnl}$ depend only on the nature of the Si crystal¹³. These Γ coefficients are of paramount importance, as they allow the determination of $\chi^{(2)}$ components in every

scenario, whatever the stress applied to silicon. However, they can only be determined from robust experiments, which were not available until now due to carrier contributions. This is a critical issue for proper optimizations of second-order nonlinear processes in silicon waveguides. In view of our set up configuration (light polarization and electric field direction), only the $\chi_{xxy}^{(2)}$ component played a major role on the detected Pockels responses, and the main two strain gradient components are η_{xxy} and η_{yyy} when applying SiN stress layer on the top of Si waveguides. Thus, Eq. (2) applied to $\chi_{xxy}^{(2)}$ can be simplified into:

$$\chi_{xxy}^{(2)}(\varphi) \simeq \Gamma_{xxy,xxy} \eta_{xxy}(\varphi) + \Gamma_{xxy,yyy} \eta_{yyy}(\varphi) \quad (3)$$

In our approach, the linear electro-optic effect (i.e., Pockels effect) in silicon was determined in high-speed regime. In this way, the frequency evolution including carriers and Pockels was taken into account. Then, an estimation of Γ coefficients could be performed by extending the model developed in ref.²⁵ to the microwave domain. The model hereafter consists the description of the S_{21} electrical signal of the electro-optic responses measured,

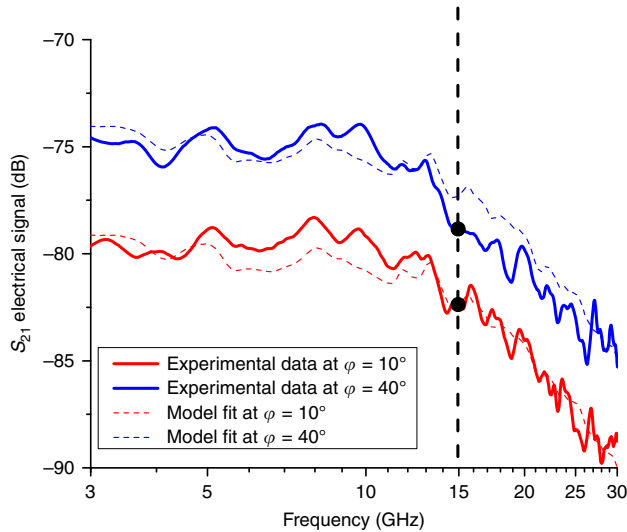


Fig. 6 Comparison between theoretical and experimental S_{21} electrical signal of the electro-optic response, between 3 GHz and 30 GHz at different orientation angles. A +15 V DC bias was applied in any case and a good agreement between experimental data and the theoretical model was achieved in all frequency

as shown in Fig. 6, in order to give an accurate value of $\chi^{(2)}$ for strained Si photonics structures. These electrical signals, R_m , in frequency domain are defined as:

$$R_m = \frac{P_{\text{out}}^{\text{AC}}}{V_{\text{in}}^{\text{AC}} Z_0} \approx \frac{P_{\text{in}} Z_0}{2 V_{\text{in}}^{\text{AC}}} \Delta\phi^{\text{AC}} \quad (4)$$

where $P_{\text{out}}^{\text{AC}}$ is the optical power at the output of the TWMZI and detected by the high-speed photodiode, $V_{\text{in}}^{\text{AC}}$ is the AC peak voltage at the input of the microwave chain, and Z_0 is the 50 Ω reference impedance. The optical power $P_{\text{out}}^{\text{AC}}$ was expressed as a function of the optical input power P_{in} and the AC optical phase shift $\Delta\phi^{\text{AC}}$ (See Methods). The expression shown in Eq. (4) includes each physical effect that play a role in the electro-optic effect, including both free-carrier plasma dispersion and Pockels effects. To extract the strain-induced Pockels effect, we consider the response from 3 GHz to 30 GHz, as it is the predominant effect in the considered frequency domain.

Using the approximation obtained in Eq. (3), the Pockels AC phase shift $\Delta\phi_p^{\text{AC}}$ can then be written as (see Methods):

$$\Delta\phi_p^{\text{AC}}(V_{\text{DC}}, \varphi, f_m) = \underbrace{\frac{2\pi}{\lambda_{\text{opt}}} \left(\Gamma_{\text{xyy,xyy}} \frac{\partial \widetilde{\eta}_{\text{xyy}}}{\partial V}(V_{\text{DC}}, \varphi, f_m) + \Gamma_{\text{xyy,yyy}} \frac{\partial \widetilde{\eta}_{\text{yyy}}}{\partial V}(V_{\text{DC}}, \varphi, f_m) \right)}_{T_{\alpha,\beta}^{(1)}(V_{\text{DC}}, \varphi, f_m)} \underbrace{\int_0^{L_{\text{arm}}} V_{\text{AC}}(z, f_m) dz}_{P^{(1)}(f_m)} \quad (5)$$

where λ_{opt} is the optical wavelength, V_{DC} the DC voltage, V_{AC} the AC voltage, f_m the microwave frequency, and $\widetilde{\eta}_{\text{mnl}}^{\text{ijk}}$ the harmonic effective strain gradients. The calculation of the term $P^{(1)}(f_m)$ was

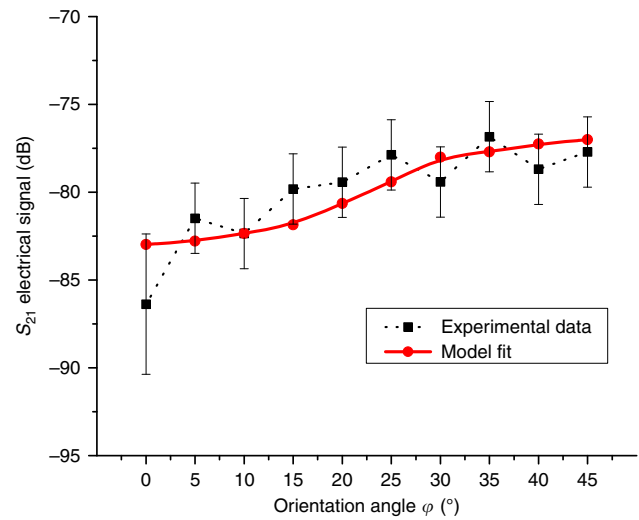


Fig. 7 S_{21} electrical signal of the theoretical and experimental electro-optic responses as a function of the orientation angle measured at 15 GHz. The error bars on the electrical signal show the maximum error made during data acquisition and are attributed to the mechanical stability of the lensed optical fiber used for light injection in the device under test. The larger error bar at $\varphi = 0^\circ$ is caused by a lower optical transmission quality observed due to fabrication imperfections on this particular device

performed by describing the AC voltage, at any position z along the TWMZI, as follows^{29–31}:

$$V_{\text{AC}}(z, f_m) = V_{\text{AC}_0}(f_m) e^{-a_m(f_m)z} \cos\left(\frac{2\pi f_m}{c} \delta_{\text{mo}}(f_m)z\right) \quad (6)$$

where V_{AC_0} is the AC voltage at the input of the TWMZI, f_m the microwave frequency, a_m the microwave loss, and $\delta_{\text{mo}}(f_m) = n_{\text{gm}}(f_m) - n_{\text{go}}(\lambda_{\text{opt}})$ is the group velocity mismatch between the microwave and the optical signals. The behavior of V_{AC_0} was determined from S-parameter measurements (see Methods). The microwave loss, a_m , was retrieved using different coplanar waveguide lengths, and the microwave group index was estimated at about 2.15, between 3 GHz and 30 GHz, due to a low dispersion of the coplanar waveguide in this frequency range. Hence, $P^{(1)}(f_m)$ mainly drives the shape of the electro-optic responses and explains the drop in modulation efficiency after 10 GHz by the group velocity mismatch between the two copropagating waves. Thus, knowing the propagative efficiency $P^{(1)}$ as a function of the microwave frequency, it is possible to fit the high-speed electro-optic results via the angle dependence and estimate both unknown coefficients $\Gamma_{\text{xyy,xyy}}$ and $\Gamma_{\text{xyy,yyy}}$.

To determine the carrier regime behavior in the silicon waveguide, high-frequency capacitance–voltage (CV) and conductance–voltage (GV) measurements were performed in order to retrieve carrier densities via the estimation of the surface fixed-charge Q_f and the interface traps D_{it} densities (see Methods). Results have shown that $Q_f \sim 10^{12} \text{ cm}^{-2}$ and $D_{\text{it}} \sim 10^{12} \text{ cm}^{-2}$. Semiconductor simulations in DC regime can be considered to describe the electric field distribution within the silicon waveguide for any DC bias applied, including the influence of Q_f and D_{it} . Furthermore, by performing harmonic perturbation-based simulations at high frequencies around a DC operating point, the distribution of the electric field in AC regime is calculated. The simulations of optical modes, strain gradients, carriers, and electric field distributions were performed using COMSOL Multiphysics software. Then, the variation of the

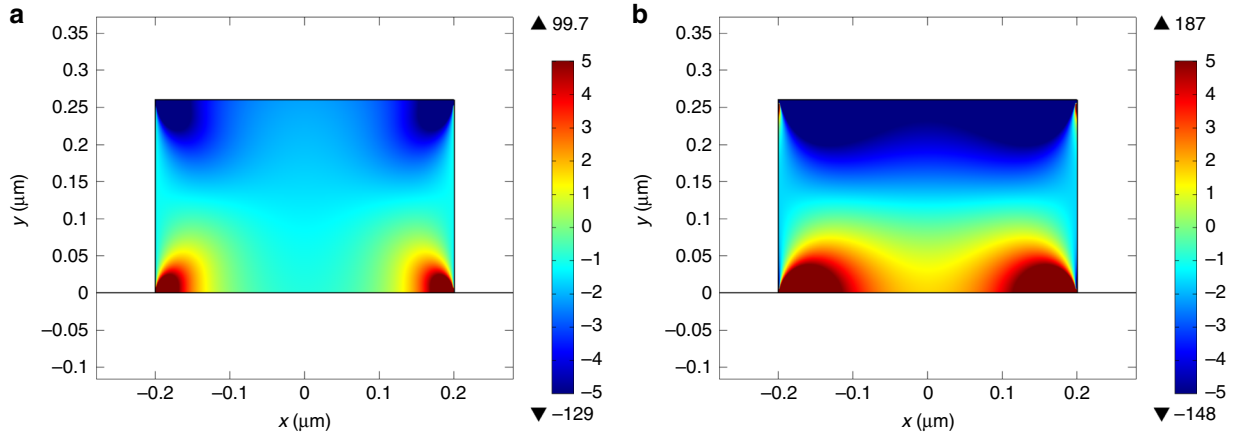


Fig. 8 $\chi_{xy}^{(2)}$ distribution (in pm V^{-1}) within the silicon waveguide using the experimentally determined Γ coefficients. **a** Along the $[0\bar{1}1]$ axis and corresponding to $\varphi = 0^\circ$. **b** Along the $[0\bar{1}0]$ axis and corresponding to $\varphi = 45^\circ$

different $\widetilde{\eta}_{mnl}^{ijk}$ with respect to the AC voltage V_{AC} is determined.

Consequently, it is possible to calculate the slopes $\frac{\partial \widetilde{\eta}_{mnl}^{ijk}}{\partial V}$ around every DC operating point and for each orientation angles φ (see Methods). Finally, by fitting experimental results from Fig. 7 with this described model, we found:

$$\begin{cases} \Gamma_{xy,xy}(\varphi) = (-4.0 \pm 0.3 + (-1.1 \pm 0.2)\cos(4\varphi)) \times 10^{-16} \text{m}^2 \text{V}^{-1} \\ \Gamma_{xy,yyy} = (-5.1 \pm 0.5) \times 10^{-16} \text{m}^2 \text{V}^{-1} \end{cases} \quad (7)$$

These values are comparable with the theoretical ones reported in¹³, indicating that our experimental approach is appropriate to describe these coefficients in strained silicon. Furthermore, we underline that both $\Gamma_{xy,xy}$ and $\Gamma_{xy,yyy}$ are unique for silicon and do not depend on the stress applied to silicon nor its orientation. Moreover a good agreement between experimental results and the model developed in this work was obtained at all frequency, as shown in Fig. 6.

Finally, the distribution in a silicon waveguide of any $\chi^{(2)}$ components is deduced using the strain gradient tensor. In Fig. 8, we determined the distribution of $\chi_{xy}^{(2)}$ in the silicon waveguide for different crystal orientations.

Discussion

First of all, it must be noted that higher $\chi_{xy}^{(2)}$ values are achieved at 45° orientation angle, corresponding here to the $[0\bar{1}0]$ crystallographic direction. This is in line with the fact that stronger strain gradients and higher $\Gamma_{ijk,mnl}$ coefficients are achieved for $\langle 100 \rangle$ equivalent directions. Furthermore, we notice that for a given orientation angle, the highest values of $\chi_{xy}^{(2)}$ (few pm V^{-1}) are only achieved at the corners of the waveguide where the strain gradients are the strongest, but their overlap with the optical mode the lowest. Due to the heterogenous behavior of $\chi_{xy}^{(2)}$ into the waveguide, an effective value of $\chi_{xy}^{(2)}$, which makes sense when describing the second-order nonlinear effects in silicon, must then be determined. This effective value is obtained by computing the overlap integral of the TE propagating mode at a wavelength of 1550 nm and the strain gradients. Hence, an effective $\chi_{xy}^{(2)}$ coefficient of $-1.8 \pm 0.2 \text{ pm V}^{-1}$ was then determined at the 45° orientation angle. In comparison, lithium niobate (LiNbO_3) and lithium tantalate (LiTaO_3) have, respectively, a nonlinear susceptibility $\chi_{xy}^{(2)}$ of 72 and -2 pm

V^{-1} , which is either comparable or one order of magnitude higher than strained silicon for this specific $\chi^{(2)}$ component. The small value achieved for strained silicon is explained by the presence of sign inversion within $\chi_{xy}^{(2)}$ distribution and a poor overlap with the mode that significantly decreases its effective value, thereby reducing the overall efficiency of second-order nonlinear processes involved. However, it is worth noting that several solutions can be developed to enhance the nonlinear efficiency in strained silicon photonics devices. The first solution consists in increasing the strain gradients by means of higher stress (greater than 2 GPa) applied to silicon using other straining materials than SiN, such as aluminum nitride (AlN), alumina (Al_2O_3), or functional oxides. Then, an optimal designed waveguide can also be considered in order to increase the overlaps between the optical mode and the strain gradients region. For instance, a strip waveguide including on its top shallow etched grooves and narrow slot may improve the strain gradient distribution and provide better overlaps with the optical mode. Asymmetric waveguides can also be a solution to better improve the strain gradient distribution according to the optical mode profile. On the other hand, increased nonlinear performances can also be obtained, depositing structured stressed layer on top of the silicon waveguide. Finally, the increase of the electric field using PIN diode in silicon could also allow achieving strong linear electro-optic effect.

In conclusion, we determined with no ambiguity a linear electro-optic effect in silicon, a well-known centrosymmetric material. A clear distinction between carrier effect and Pockels effect was achieved for the first time in high-speed regime. Besides, we characterized the strain-induced $\chi^{(2)}$ tensor in silicon through the measurements of Pockels responses in the microwave regime. A multiphysics model has been developed in order to accurately describe these frequency responses and extract critical coefficients (i.e., the $\Gamma_{ijk,mnl}$ coefficients) necessary for the complete identification of each $\chi^{(2)}$ components with respect to the strain gradient distributions induced in a silicon waveguide. Hence, this model allowed the calculation of an effective value of $-1.8 \pm 0.2 \text{ pm V}^{-1}$ for the $\chi_{xy}^{(2)}$ component for a conventional silicon strip waveguide strained by SiN. Finally, we want to highlight that the knowledge of the unique $\Gamma_{ijk,mnl}$ coefficients paves the way for the optimization of silicon-based photonic structures. Considering a stressed layer of 5 GPa, which is not the maximum value achievable in silicon, and an optimized strain gradient distribution into the silicon waveguide, more than 100 pm V^{-1} may be reached, suitable for efficient light modulation.

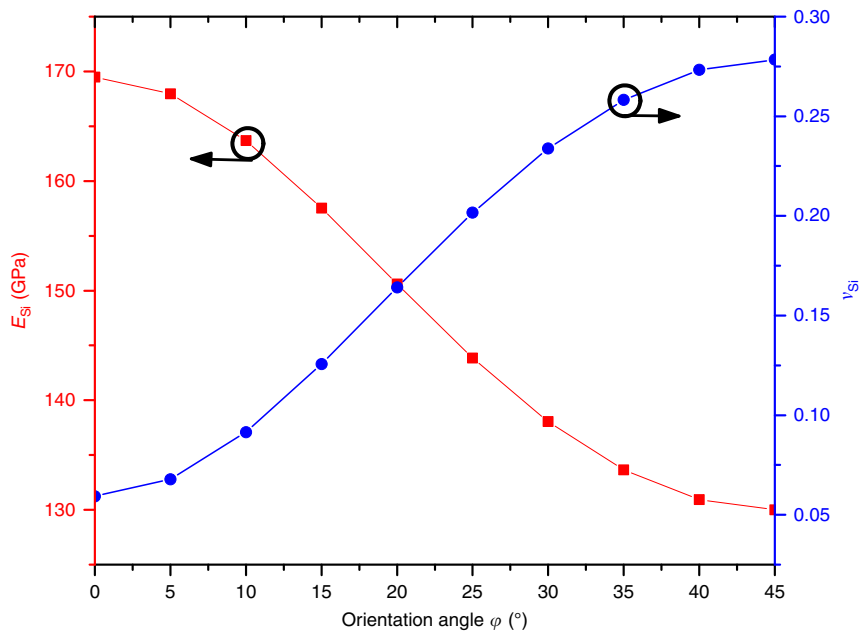


Fig. 9 Young's modulus E_{si} and Poisson's ratio ν_{si} of silicon as a function of the traveling-wave Mach-Zehnder interferometer (TWMZI) orientation φ

Methods

Sample fabrication. The device was fabricated using a p-type high-resistivity SOI wafer with a 260-nm-thick silicon film on a 2- μm -thick silicon dioxide. A first electron beam lithography was performed to define the waveguides in a ZEP e-beam resist. Then, fully etched waveguides were obtained using an inductively coupled plasma etching technique. A 700-nm-thick highly stressed ($\sigma_i = -1.3$ GPa) silicon nitride was deposited by plasma enhanced chemical vapor deposition (PECVD) technique in order to strain the silicon waveguides. A second lithography level was performed to define the coplanar electrodes. A 500-nm-thick gold layer was evaporated all over the sample and lifted-off away to make the traveling-wave electrodes. Finally, the samples were cleaved to enable the optical edge coupling measurements.

High-speed measurements setup. High-speed measurements were carried out to obtain the electro-optic response of TWMZI as a function of the RF/microwave electric signal frequency.

A S-parameters test set combined with a lightwave component analyzer (LCA) was used to generate a RF electric signal, with a frequency variation from 100 MHz to 40 GHz. This electric signal was subsequently amplified using a RF modulator driver working between 40 kHz and 38 GHz before being injected into a traveling-wave coplanar electrode via GSG-based RF probes. Two bias tees were added, one between the output of the RF modulator driver and the input GSG-based RF probes, and the other after the output GSG-based RF probes. A DC bias between -15 V and $+15$ V could be superimposed with the RF signal in order to modify the carrier regime within the silicon waveguide. The RF signal propagated through the circuit until a 50Ω load, while the DC bias was applied in an open circuit to avoid high electric current along the electrodes.

In parallel, a continuous wavelength tunable laser working in the C-band was employed to inject a TE-polarized optical signal through the use of a lensed optical fiber. A total of 90% of the output power was then coupled to the LCA, while the remaining 10% was detected by an optical component power meter to retrieve the optical transmission of the Mach-Zehnder interferometers.

The modulated optical signal was detected by a high-speed photodiode included inside the LCA and converted into an electrical signal. The later was then normalized by the input electrical signal generated from the S-parameters test set and the result was plotted on a vector network analyzer to read and characterize the electro-optic response of the modulator.

$$R_m = \frac{P_{out}^{AC}}{I_{in}^{AC}} = \frac{P_{out}^{AC}}{V_{in}^{AC}} Z_0 \quad (8)$$

where P_{out}^{AC} is the optical power at the output of the TWMZI and detected by the high-speed photodiode, I_{in}^{AC} is the AC peak intensity, V_{in}^{AC} is the AC peak voltage at the input of the microwave chain, and Z_0 is the 50Ω reference impedance.

All the RF components were separately characterized between 100 MHz and 40 GHz with a S-parameters test set. The calibration was performed using a SOLT (short-open-load-thru) tool kit.

Characterization of surface fixed-charges and interface traps densities through CV and GV measurements

The off-load silicon electronic configuration is known via the characterization of the surface fixed-charges Q_f and interface traps D_{it} densities. Indeed, positive charges are present in the SiN cladding around the silicon waveguide and consequently a constant electric field is applied to the waveguide, moving carriers to the inversion regime. Furthermore, interface traps, caused by defects at the Si/SiN interface, creating new energy levels in the silicon band gap, alter the re-distribution of carriers under a DC bias. High-frequency capacitance-voltage (CV) and conductance-voltage (GV) measurements of stressed SiN insulator layers on silicon substrate were performed to calculate Q_f and D_{it} , using methods described in ref.³².

Silicon mechanical anisotropy. Silicon being an anisotropic mechanical material, its Young's modulus and Poisson's ratio are varying according to the crystal orientation³³, as shown in Fig. 9. When the angle of the waveguide increases in reference of the $[0\bar{1}1]$, Young's modulus and Poisson's ratio are, respectively, decreasing and increasing. This means that silicon becomes more easily strained and deformed by a given level of external stress.

Expression of the optical power at the output of the DUT using the MZI transfer function

The MZI transfer function is expressed as:

$$P_{out} = \frac{P_{in}}{2} (1 + \cos(\Delta\phi)) \quad (9)$$

where P_{out} is the output optical power of the MZI, P_{in} the input optical power, and $\Delta\phi$ is the optical phase shift between the two arms. The later can be decomposed as the sum of a DC component $\Delta\phi^{DC}$ (that also takes into account the initial asymmetry of the MZI) and an AC component $\Delta\phi^{AC}$. Indeed in our experiment, the voltage applied to the electrodes is a combination of a DC bias and an AC signal, and both of them induced electro-optic effects. Because every measurements were performed at quadrature operating points (where the transfer function is linearized), Eq. (9) is simplified into:

$$P_{out} = \frac{P_{in}}{2} \pm \frac{P_{in}}{2} \Delta\phi^{AC} = P_{out}^{DC} + P_{out}^{AC} \quad (10)$$

Expression of Γ coefficients. In ref.¹³, it has been reported that the $\Gamma_{ijk,mnl}$ coefficients can be expressed as a function of two unknown parameters α and β . In our experiments, only $\Gamma_{xxy,xyy}$ and $\Gamma_{xyx,yyy}$ are needed to describe the main component responsible for Pockels responses, i.e., $\chi_{xxy}^{(2)}$. They are written hereafter:

$$\begin{cases} \Gamma_{xxy,xyy}(\varphi) = \frac{d^2K}{27\epsilon_0} (5\beta - 3\alpha - (\alpha + \beta)\cos(4\varphi)) \\ \Gamma_{xyx,yyy} = -\frac{d^2K}{27\epsilon_0} (2(\alpha - 3\beta)) \end{cases} \quad (11)$$

with $d = 0.235$ nm the distance between the atoms in the silicon lattice, $K = -1.18 \times 10^{29} \text{ C}^3 \text{ m}^{-3} \text{ eV}^{-313}$ and φ the TWMZI orientation angle.

Modeling description of optical phase shift induced by Pockels effect in AC regime. The optical phase shift $\Delta\phi_p$ induced by Pockels effect along the arm of one φ -angled MZI is expressed as:

$$\Delta\phi_p(\varphi) = \int_0^{L_{\text{arm}}} \frac{2\pi}{\lambda_{\text{opt}}} \Delta n_{\text{eff},p}(z, \varphi) dz \quad (12)$$

The effective index change $\Delta n_{\text{eff},p}$ was described using the method employed in ref.²⁵, which combined the perturbation theory for waveguides with the description of strain-induced $\chi^{(2)}$. Hence, under an arbitrary voltage $V(z)$ we have

$$\Delta n_{\text{eff},p}(z, \varphi) = \sum_{ijk} \sum_{mnl} \Gamma_{ijk,mnl} \widehat{\eta}_{mnl}^{ijk}(V(z), \varphi) \quad (13)$$

where $\widehat{\eta}_{mnl}^{ijk}$ are the effective strain gradients, describing the overlap between the mode profile, each strain gradient tensor components η_{mnl} and the electric field induced by the electrodes. Such overlaps are written

$$\widehat{\eta}_{mnl}^{ijk}(V(z), \varphi) = \frac{2c\epsilon_0}{N} \int_{\text{wg}} \eta_{mnl}(\varphi) E_i E_j F_k(V(z)) dS \quad (14)$$

where the parameter N is given by

$$N = \int_{\infty} (\mathbf{E} \times \mathbf{H}^* + \mathbf{E}^* \times \mathbf{H}) \cdot \mathbf{z} dS \quad (15)$$

and corresponds to the active power of the optical mode.

During the high-speed experiments performed, the voltage applied at a position z along the electrode was a combination of a DC bias and a microwave AC voltage with frequency f_m

$$V(z) = V_{\text{DC}} + V_{\text{AC}}(z, f_m) \quad (16)$$

The DC bias V_{DC} allowed the modification of the carriers regime and in turn the electric field within the silicon waveguide while the AC component V_{AC} was used to probe the response of Pockels effect at high frequencies around that DC operating point. A first-order Taylor expansion can be performed around the DC operating point such that the effective strain gradients can be decomposed into a DC and an AC term as follows

$$\widehat{\eta}_{mnl}^{ijk}(V(z), \varphi) \simeq \widehat{\eta}_{mnl}^{ijk}(V_{\text{DC}}, \varphi) + V_{\text{AC}}(z, f_m) \frac{\partial \widehat{\eta}_{mnl}^{ijk}}{\partial V}(V_{\text{DC}}, \varphi, f_m) \quad (17)$$

where $\widehat{\eta}_{mnl}^{ijk}$ is the harmonic effective strain gradient calculated considering V_{AC} as a harmonic perturbation. By combining Eqs. (13) and (17) the Pockels-based effective index change can be expressed as the sum of a DC bias $\Delta n_{\text{eff},p}^{\text{DC}}$ and an AC component $\Delta n_{\text{eff},p}^{\text{AC}}$. The later is expressed

$$\Delta n_{\text{eff},p}^{\text{AC}}(V_{\text{DC}}, \varphi, z, f_m) = \left(\sum_{ijk} \sum_{mnl} \Gamma_{ijk,mnl} \frac{\partial \widehat{\eta}_{mnl}^{ijk}}{\partial V}(V_{\text{DC}}, \varphi, f_m) \right) V_{\text{AC}}(z, f_m) \quad (18)$$

By integrating equation (18) along the interaction zone of the TWMZI, as showed by equation (12), we may write the phase change induced through Pockels effect $\Delta\phi_p^{\text{AC}}$ as

$$\Delta\phi_p^{\text{AC}}(V_{\text{DC}}, \varphi, f_m) = \frac{2\pi}{\lambda_{\text{opt}}} \underbrace{\left(\sum_{ijk} \sum_{mnl} \Gamma_{ijk,mnl} \frac{\partial \widehat{\eta}_{mnl}^{ijk}}{\partial V}(V_{\text{DC}}, \varphi, f_m) \right)}_{T_{\alpha\beta}^{(1)}(V_{\text{DC}}, \varphi, f_m)} \underbrace{\int_0^{L_{\text{arm}}} V_{\text{AC}}(z, f_m) dz}_{P^{(1)}(f_m)} \quad (19)$$

$T_{\alpha\beta}^{(1)}$ and $P^{(1)}$ represent the transverse Pockels efficiency and the propagative Pockels efficiency respectively. Both terms depict how the microwave modulation is transferred to the optical wave.

Data availability

The data that support the findings of this study are available from the corresponding author upon reasonable request.

Received: 19 April 2018 Accepted: 12 September 2018

Published online: 12 October 2018

References

- Fedeli, J. M. et al. Development of silicon photonics devices using microelectronic tools for the integration on top of a cmos wafer. *Adv. Opt. Technol.* **2008**, 1–15 (2008).
- Leuthold, J., Koos, C. & Freude, W. Nonlinear silicon photonics. *Nat. Photonics* **4**, 535–544 (2010).
- Arizmendi, L. Photonic applications of lithium niobate crystals. *Phys. Status Solidi (a)* **201**, 253–283 (2004).
- Rabiei, P., Ma, J., Khan, S., Chiles, J. & Fathpour, S. Heterogeneous lithium niobate photonics on silicon substrates. *Opt. Express* **21**, 25573 (2013).
- Wang, C., Zhang, M., Stern, B., Lipson, M. & Loncar, M. Nanophotonic lithium niobate electro-optic modulators. *Opt. Express* **26**, 1547 (2018).
- Bogdanov, S., Shalaginov, M. Y., Boltasseva, A. & Shalae, V. M. Material platforms for integrated quantum photonics. *Opt. Mater. Express* **7**, 111 (2017).
- Govorkov, S. V., Koroteev, N. I., Petrov, G. I., Shumay, I. L. & Yakovlev, V. V. Laser nonlinear-optical probing of silicon/SiO₂ interfaces: Surface stress formation and relaxation. *Appl. Phys. A Solids Surf.* **50**, 439–443 (1990).
- Huang, J. Y. Probing inhomogeneous lattice deformation at interface of Si (111)/SiO₂ by optical second-harmonic reflection and Raman spectroscopy. *Jpn. J. Appl. Phys.* **33**, 3878–3886 (1994).
- Hon, N. K., Tsia, K. K., Solli, D. R. & Jalali, B. Periodically poled silicon. *Appl. Phys. Lett.* **94**, 091116 (2009).
- Cazzanelli, M. et al. Second-harmonic generation in silicon waveguides strained by silicon nitride. *Nat. Mater.* **11**, 148–154 (2012).
- Manganelli, C. L., Pintus, P. & Bonati, C. Modeling of strain-induced Pockels effect in Silicon. *Opt. Express* **23**, 28649 (2015).
- Luppi, E., Degoli, E., Bertocchi, M., Ossicini, S. & Vénier, V. Strain-designed strategy to induce and enhance second-harmonic generation in centrosymmetric and noncentrosymmetric materials. *Phys. Rev. B* **92**, 075204 (2015).
- Damas, P., Marris-Morini, D., Cassan, E. & Vivien, L. Bond orbital description of the strain-induced second-order optical susceptibility in silicon. *Phys. Rev. B* **93**, 165208 (2016).
- Jacobsen, R. S. et al. Strained silicon as a new electro-optic material. *Nature* **441**, 199–202 (2006).
- Chmielak, B. et al. Pockels effect based fully integrated, strained silicon electro-optic modulator. *Opt. Express* **19**, 17212 (2011).
- Chmielak, B. et al. Investigation of local strain distribution and linear electro-optic effect in strained silicon waveguides. *Opt. Express* **21**, 25324 (2013).
- Damas, P. et al. Wavelength dependence of Pockels effect in strained silicon waveguides. *Opt. Express* **22**, 22095 (2014).
- Puckett, M. W., Smalley, J. S. T., Abashin, M., Grieco, A. & Fainman, Y. Tensor of the second-order nonlinear susceptibility in asymmetrically strained silicon waveguides: analysis and experimental validation. *Opt. Lett.* **39**, 1693 (2014).
- Borghini, M. et al. High-frequency electro-optic measurement of strained silicon racetrack resonators. *Opt. Lett.* **40**, 5287 (2015).
- Soref, R. & Bennett, B. Electrooptical effects in silicon. *IEEE J. Quantum Electron.* **23**, 123–129 (1987).
- Reed, G. T., Mashanovich, G., Gardes, F. Y. & Thomson, D. J. Silicon optical modulators. *Nat. Photonics* **4**, 518–526 (2010).
- Sharif Azadeh, S., Merget, F., Nezhad, M. P. & Witzens, J. On the measurement of the Pockels effect in strained silicon. *Opt. Lett.* **40**, 1877 (2015).
- Sharma, R., Puckett, M. W., Lin, H.-H., Vallini, F. & Fainman, Y. Characterizing the effects of free carriers in fully etched, dielectric-clad silicon waveguides. *Appl. Phys. Lett.* **106**, 241104 (2015).
- Olivares, I., Angelova, T. & Sanchis, P. On the influence of interface charging dynamics and stressing conditions in strained silicon devices. *Sci. Rep.* **7**, 7241 (2017).
- Damas, P. et al. Comprehensive description of the electro-optic effects in strained silicon waveguides. *J. Appl. Phys.* **122**, 153105 (2017).
- Lin, H. et al. Breaking the energy-bandwidth limit of electrooptic modulators: theory and a device proposal. *J. Light. Technol.* **31**, 4029–4036 (2013).
- Muller, J. Thin Silicon Film p-i-n Photodiodes with Internal Reflection. *IEEE J. Solid-State Circuits* **13**, 173–179 (1978).
- Xu, Q., Schmidt, B., Pradhan, S. & Lipson, M. Micrometre-scale silicon electro-optic modulator. *Nature* **435**, 325–327 (2005).
- Alfèrness, R. Waveguide Electrooptic Modulators. *IEEE Trans. Microw. Theory Tech.* **30**, 1121–1137 (1982).
- Alfèrness, R., Korotky, S. & Marcattili, E. Velocity-matching techniques for integrated optical traveling wave switch/modulators. *IEEE J. Quantum Electron.* **20**, 301–309 (1984).
- Ghione, G. *Semiconductor devices for high-speed optoelectronics* (Cambridge University Press 2009).
- Sze, S. M. & Ng, K. K. *Physics of semiconductor devices* (Wiley-Interscience 2007).

33. Wortman, J. J. & Evans, R. A. Young's Modulus, Shear Modulus, and Poisson's Ratio in Silicon and Germanium. *J. Appl. Phys.* **36**, 153–156 (1965).

Acknowledgements

This project has received funding from the European Research Council (ERC) under the European Union's Horizon 2020 research and innovation program (ERC POPSTAR - grant agreement No 647342). Authors thank Jean-Marc Fedeli from CEA/LETI, France for its technical help, and Frederic Boeuf and Charles Baudot from STMicroelectronics for their support in strained silicon photonics developments. The fabrication of the devices was performed at the technological nano-center of C2N, which was partially funded by the Conseil Général de l'Essonne. This work was supported by the French RENATECH network. D.M.-M. acknowledges support by the Institut Universitaire de France.

Author contributions

X.L.R. and M.B. fabricated the samples and developed the Si strained process with the help of P.D. and G.M. D.B. helped M.B. with the optical coupling of light in the samples. P.C., D.M.M., and M.B. performed microwave electrical characterizations of the coplanar waveguides and RF devices. Electro-optic measurements were carried out by M.B. with the help of D.P.G., C.A.R., and L.V. M.B. developed the high-speed model with the help of P.C. and E.C. L.V. initiated and supervised the research project. All authors discussed the results and contributed to writing the manuscript.

Additional information

Competing interests: The authors declare no competing interests.

Reprints and permission information is available online at <http://npg.nature.com/reprintsandpermissions/>

Publisher's note: Springer Nature remains neutral with regard to jurisdictional claims in published maps and institutional affiliations.



Open Access This article is licensed under a Creative Commons Attribution 4.0 International License, which permits use, sharing, adaptation, distribution and reproduction in any medium or format, as long as you give appropriate credit to the original author(s) and the source, provide a link to the Creative Commons license, and indicate if changes were made. The images or other third party material in this article are included in the article's Creative Commons license, unless indicated otherwise in a credit line to the material. If material is not included in the article's Creative Commons license and your intended use is not permitted by statutory regulation or exceeds the permitted use, you will need to obtain permission directly from the copyright holder. To view a copy of this license, visit <http://creativecommons.org/licenses/by/4.0/>.

© The Author(s) 2018